Materials Advances

Accepted Manuscript

This article can be cited before page numbers have been issued, to do this please use: D. B. Niranjan, M. Peter, J. Medikonda and P. Namboothiri, *Mater. Adv.*, 2025, DOI: 10.1039/D4MA01258E.

ROYAL SOCIETY OF CHEMISTRY

rsc.li/materials-advances

View Article Online
DOI: 10.1039/D4MA01258E

ARTICLE

Development of face mask attachable wireless piezoresistive nanocomposite sensor for monitoring respiratory health

Received 00th January 20xx,
Accepted 00th January 20xx

DOI: 10.1039/x0xx00000x

Niranjan D B[a], Mathew Peter[a], Jeevan Medikonda[a] and Pramod Kesavan Namboothiri[a]*

A piezoresistance-based stretchable nanocomposite strip, which can be attached to a face mask, has been developed. The wireless acquisition of respiratory activities using this nanocomposite strip is demonstrated. PU/f-MWCNT (Polyurethane/functionalized- Multiwall carbon nanotubes) nanocomposite was prepared by functionalizing MWCNTs and integrating them with PU. The functionalization of MWCNTs was confirmed by FTIR analysis. A study on the effect of carboxylic functionalization of MWCNTs on the dispersion of MWCNTs in the PU matrix was carried out by measuring resistance at different regions of the nanocomposite. It was observed that carboxylic functionalized CNTs dispersed uniformly in the PU matrix compared to non-functionalized MWCNTs. The electrical percolation threshold was achieved at 1.8 % concentration of f-MWCNTs for the nanocomposites. The nanocomposites were further used to fabricate a wearable sensor for sensor- enabled mask , which could acquire respiratory patterns in real-time. The sensor can identify respiratory patterns, such as the mean time required to complete one respiration cycle. In normal breathing, the average time to complete one respiratory cycle was 3.44 seconds, with a pause of 0.73 sec-onds between consecutive cycles. However, for slow breathing patterns, the time required to complete one cycle increased to 7.05 seconds, and the hold time between cycles increased to 2 seconds. Identifying respiratory signal patterns helps identify inhalation and exhalation durations, which helps identify dysfunctional respiration. The developed sensor enabled sensor- enabled mask is suitable for continuous remote monitoring of respiratory disorders outside the clinical setting. Continuous monitoring of respiratory health can be beneficial for timely intervention or for monitoring respiratory illness and recovery.

1. Introduction

Recent developments in wearable sensor field have reformed biomedical applications by enabling continuous, non-invasive (or minimally invasive) monitoring of vital bodily functions such as heart rate, glucose levels, and physical activity [1-5]. Leveraging innovations in flexible electronics, self powered, wide detection range, compact hardware design, and wireless communication, these devices are engineered for unobtrusive, comfortable wear and allows real-time data that is crucial for both clinical assessments and personal health management[6-10]. This continuous monitoring capability supports early disease detection, effective management of chronic conditions, and personalized healthcare strategies. By bridging the gap between conventional diagnostic methods and everyday health tracking, wearable sensors are paving the way for a more patient-focussed approach in modern medicine, fundamentally transforming preventive care[11-15]. In this regard, conductive polymer nanocomposites based stretchable strain sensors have gained attention in fabricating wearable gadgets for continuous monitoring. Strain sensors are significant for monitoring a wide range of activities ranging from motion capture to healthcare applications[16-17]. Different types of conductive nanomaterials, including two-dimensional graphene nanoplatelets, one-dimensional carbon nanotubes, zero-dimensional metal nanoparticles, and carbon black, are utilized to enhance polymer matrices like silicone rubber, polydimethylsiloxane, and polyurethane [18-22]. Advances in stretch sensors can enable the fabrication of smart wearable sensors for remote monitoring and real-time analysis of patients for healthcare applications. In pandemic-like situations (such as coronavirus disease, MERS, or Influenza), parameters like respiratory rate are used to assess a patient's clinical status and predict the severity of illness [23-27]. More than half of the patients develop respiratory symptoms such as shortness of breath and wheezing, leading to more severe complications like pneumonia. In such situations, noncontact-based or remote monitoring helps prevent the spread of disease to healthcare professionals. This method of assessing respiratory patterns minimizes contact between clinicians and patients and, at the same time, helps in monitoring respiratory health in affected patients. Noncontact-based monitoring can aid in identifying early signs of the development of respiratory complications in

[a] Department of Biomedical Engineering, Manipal Institute of Technology, Manipal, Manipal Academy of Higher Education, Manipal, 576104, India

Corresponding author email address: pramod.kn@manipal.edu

Supplementary Information available: Circuit program for acquiring signals provided and Respiratory acquisition demo from sensor enabled mask uploaded as video. See DOI: 10.1039/x0xx00000x

View Article Online
DOI: 10.1039/D4MA01258E

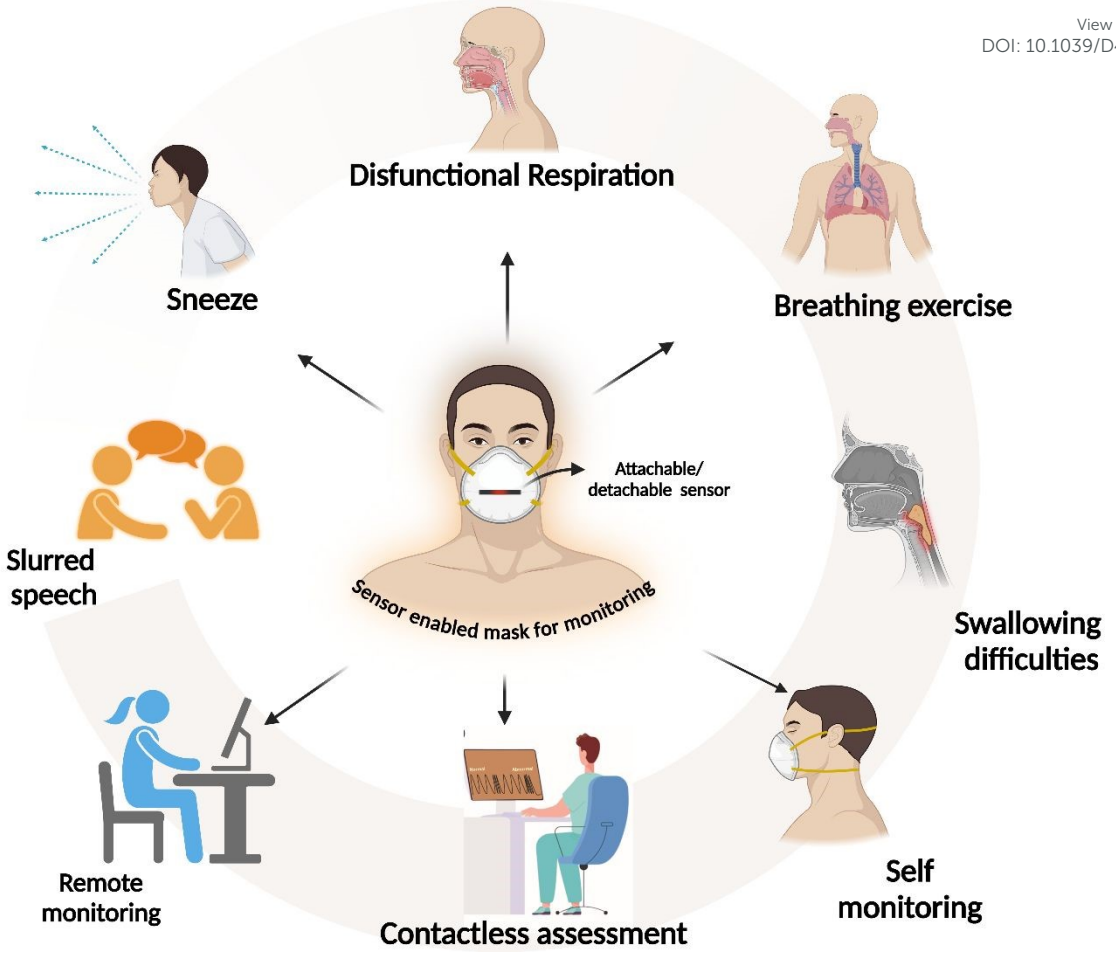

Figure 1: Overview of prepared sensor enabled mask applications and its versatility

patients. Several methods are currently used for evaluating respiratory health, as pulmonary function tests range from simple spirometry to assess airflow to whole-body plethysmography, which provides lung volume [28]. However, these methods need a laboratory setting to understand respiratory health and are unsuitable for continuous remote monitoring for long durations. Continuous respiration monitoring is achieved through different methods. In respiratory inductive plethysmography (RIP), two inductive belts are used around the abdomen and ribcage to measure the changes in circumference during respiration and determine the respiratory volume. Kono and Mead developed this volume measurement concept in 1967, which has since been well-established for monitoring patients in a clinical setting [29]. Like the RIP method, cameras or depth and acoustic-based sensors can be used to evaluate the patient's respiratory activity. Optoelectronic plethysmography measures respiratory activity by acquiring the movement of the patient's torso from the reflectors placed using several cameras[30]. Another method used is the measurement of transthoracic impedance by placing different electrodes [31] These methods of continuous respiratory monitoring require specialized equipment or infrastructure, which may not be suitable for remote monitoring. Researchers fabricated devices for monitoring vital signs, however not many studies re-ported on polymer nanocomposite-based breath activity monitoring sensor.[32-36]

In this paper we present proof-of-concept for the preparation of piezoresistive nanocomposite strips that can be attached to the patient's mask to convert it into a sensor-enabled mask , as shown in Figure 1 to monitor respiratory health. During inhalation and exhalation from the nostrils, direct pressure is built on nanocomposites, which disrupts the conducting path of MWCNTs in the composites and changes resistance. The change in resistance is recorded and transmitted wirelessly through a mobile or a computer terminal. The data obtained from the sensor- enabled mask is processed, analyzed, and correlated, and finally, the patient's current stage is evaluated.

2. Materials: Pristine multiwall carbon nanotube (p-MWCNT) produced by the carbon vapor deposition method (CVD) with a purity of ~99% purchased from Adnano Technologies Pvt ltd., Shimoga, India, and matrix material polyurethane sup-plied M/s VCM Polyurethane Pvt. Ltd. Mumbai, India. Chemical reagents Nitric acid (HNO_3, 65%) was purchased from Sigma- Aldrich. Milli-Q (DI) water was used for all the preparations.

View Article Online
DOI: 10.1039/D4MA01258E

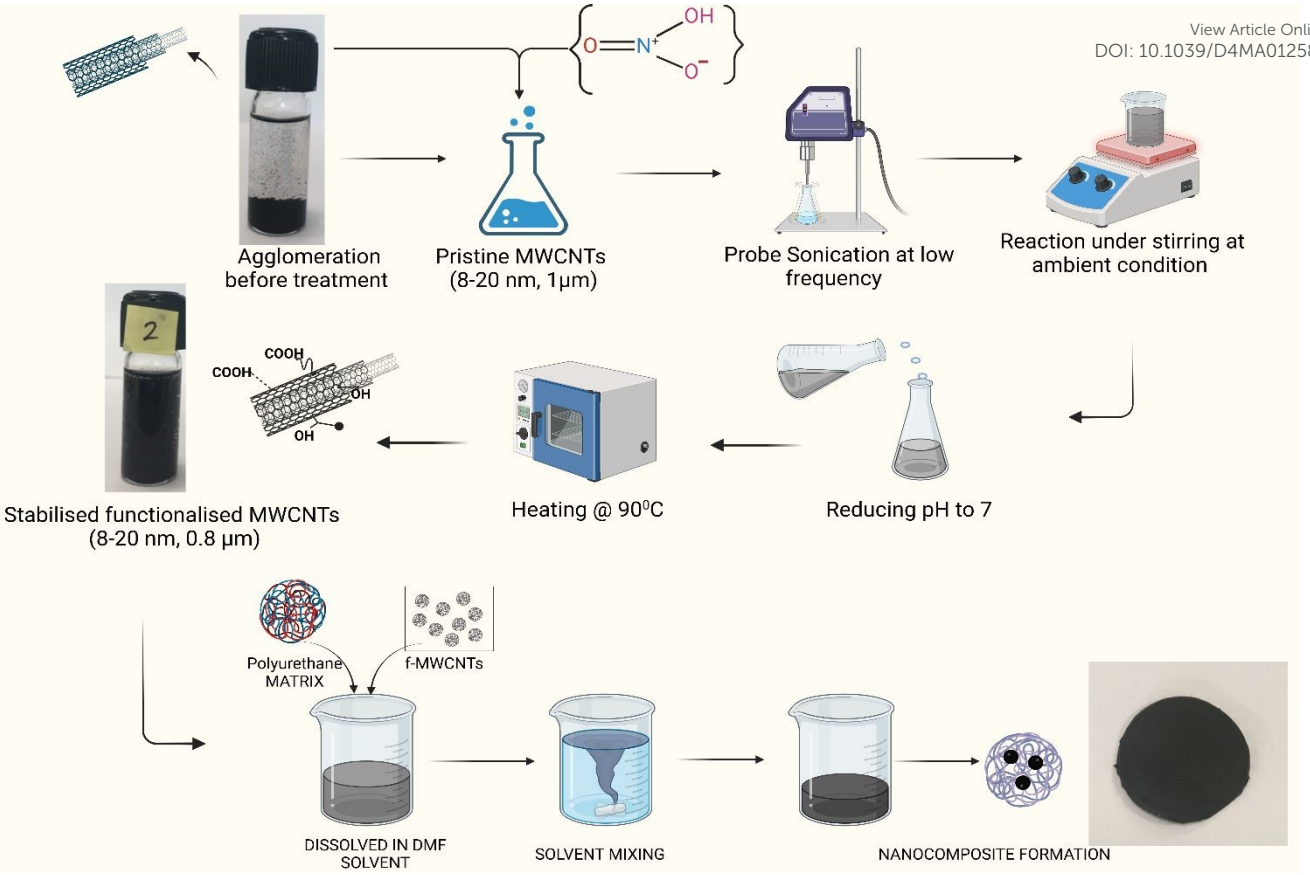

Figure 2: Functionalization of p-MWCNTs by acid oxidation method to prepare nanocomposite

3. Result and Discussion

3.1. Surface modification of p-MWCNTs*:* The surface modification of p-MWCNTs was carried out using the acid modification method in which p-MWCNTs were treated with acids and dispersed in solvents. In the acid oxidation method, p-MWCNTs are treated with acids or oxidizing agents, such as HNO_3, H_2SO_4, a mixture of HNO_3 and H_2SO_4, $KMnO_4$, H_2O_2 and $(NH_4)_2S_2O_8$, etc.[37] The several types of surface groups play various functions based on the requirement. Several authors reported using a mixture of HNO_3 with H_2SO_4 in different ratios to treat p-MWCNTS under sonication. As per the literature, treating p-MWCNTs with acids can lead to different surface modifications and defects. The treatment of p-MWCNTs with nitric acid results in the carboxylation of side wall and end caps, and at higher concentrations of nitric acid, can also cause more damage to f-MWCNTs by breaking them into shorter pieces, resulting in a change in aspect ratio[38]. Another study reported the shortening of MWNCTs by ultra-sonic treatment in a mixture of H_2SO_4 and HNO_3[39]. Osorio et al.[40] showed no significant change for a short time when CNTs were exposed to the nitric acid environment. However, long-time exposure increases the carboxyl, C-O, and hydroxyl groups on the side walls of MWCNTs. For the adsorption of COOH and =O, Shanmugharaj et al. [41]. immersed CNTs in sulfuric acid and potassium dichromate at 80°C for 30 min. However, treating CNTs for an extended duration resulted in the shortening of CNTs. All these studies show that attaching COOH groups and defect formation on MWCNTs by acid oxidation relies mainly on concentration, reaction time, and temperature.

In this work, to reduce more damage to p-MWCNTs, the treatment conditions were optimized by keeping reaction time and the temperature constant and varying concentration. Nitric acid concentration varied from 1M to 7M. Figure 2 depicts the procedure adopted for functionalization. To functionalize p-MWCNTs with COOH groups, 0.1 g of MWCNTs were dispersed in 50 ml of different molar concentrations of HNO_3. The mixture was probe-sonicated for 2 hours at 5% of 20kHz and after that stirred for 4 hours at ambient conditions. After treatment, functionalized MWCNTs (f-MWCNTs) were washed to remove acid traces using Milli-Q water till the pH became 7. f-MWNCTs were dried at 90˚C overnight in a vacuum oven to remove water content.

The surface-modified MWCNTs were further used to prepare nanocomposites using the solution casting method. In this method, polymer and filler materials are dispersed in the solution and cast in a petri dish or mold to evaporate and form the nanocomposite. Proper filler (f-MWCNTs) dispersion in the

View Article Online
DOI: 10.1039/D4MA01258E

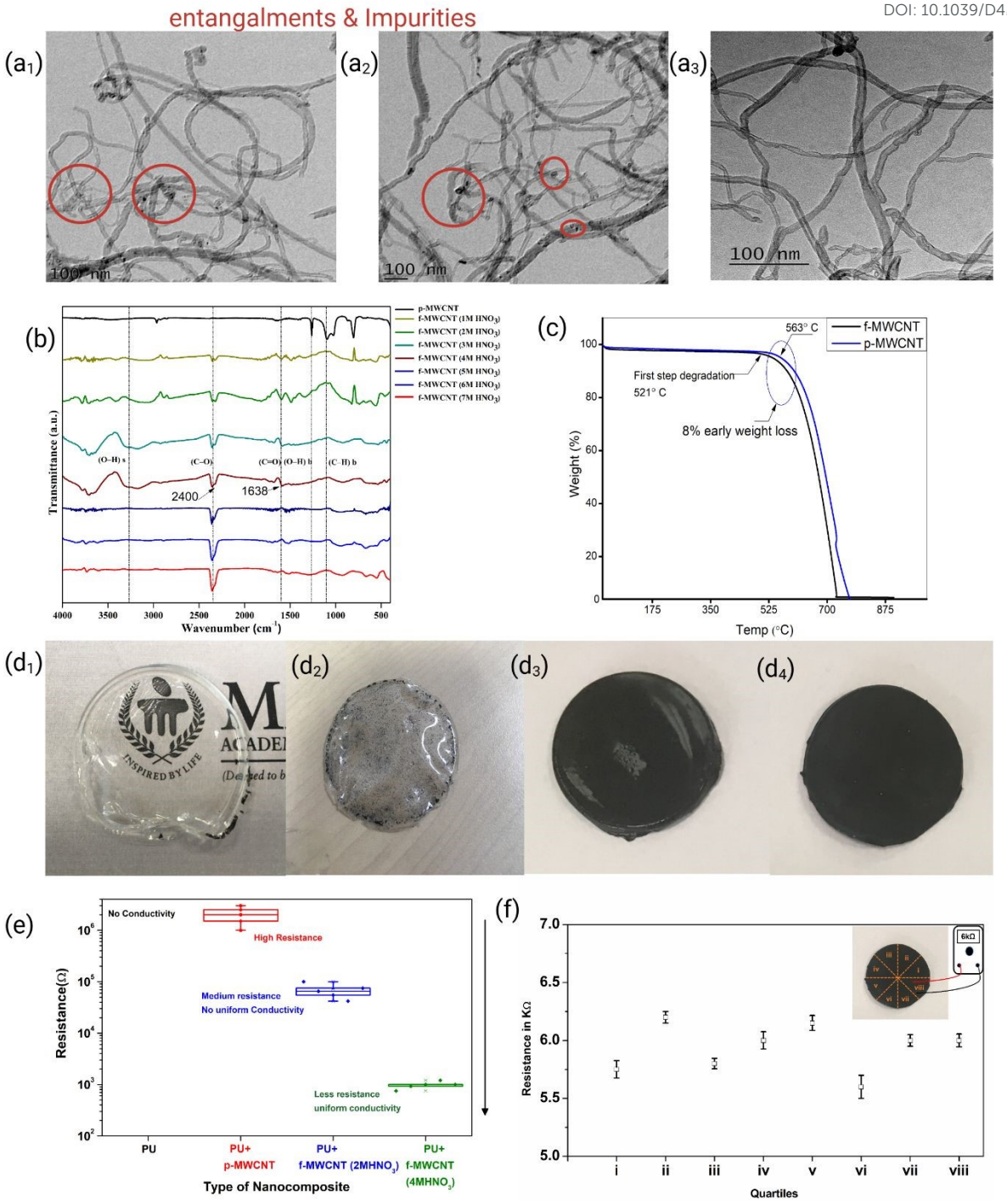

Figure 3:(a_1-a_3) shows the TEM image of p-MWCNTs and f-MWCNTs, (b) shows the FTIR spectra of acid functionalization, (c) shows TGA curves of MWCNTs , (d_1-d_4) shows PU and its nanocomposites, (e) shows the resistance change for different filler loading to nanocomposites and (f) shows uniform electrical property on nanocomposite.

polymer matrix is crucial in this process. Therefore, surface modification of MWCNTs with COOH groups is essential to achieve uniform dispersion of fillers in solvents.

3.2. Characterization of MWCNTs and Nanocomposites: The morphology of p-MWCNT and f-MWCNTs was analysed using transmission electron microscopy (TEM), as shown in figure 3 (a). TEM images showed that the outer diameter of p-MWCNTs is 10-30 nm, inner diameter 5-10 nm, and length >1 µm. An IRSpirit Shimadzu-made instrument was used for the FTIR study. TGA curves of p-MWCNT and f-MWCNT) are shown in figure 3.

TGA analysis was performed under N_2 flow, at a heating rate of 10°C/min. Figure 3 (b) shows the FTIR spectra of the f-MWCNTs after acids treatment. For this experiment, the concentration of HNO_3 varied from 1M to 7M. The peak observed for f-MWCNTs

View Article Online
DOI: 10.1039/D4MA01258E

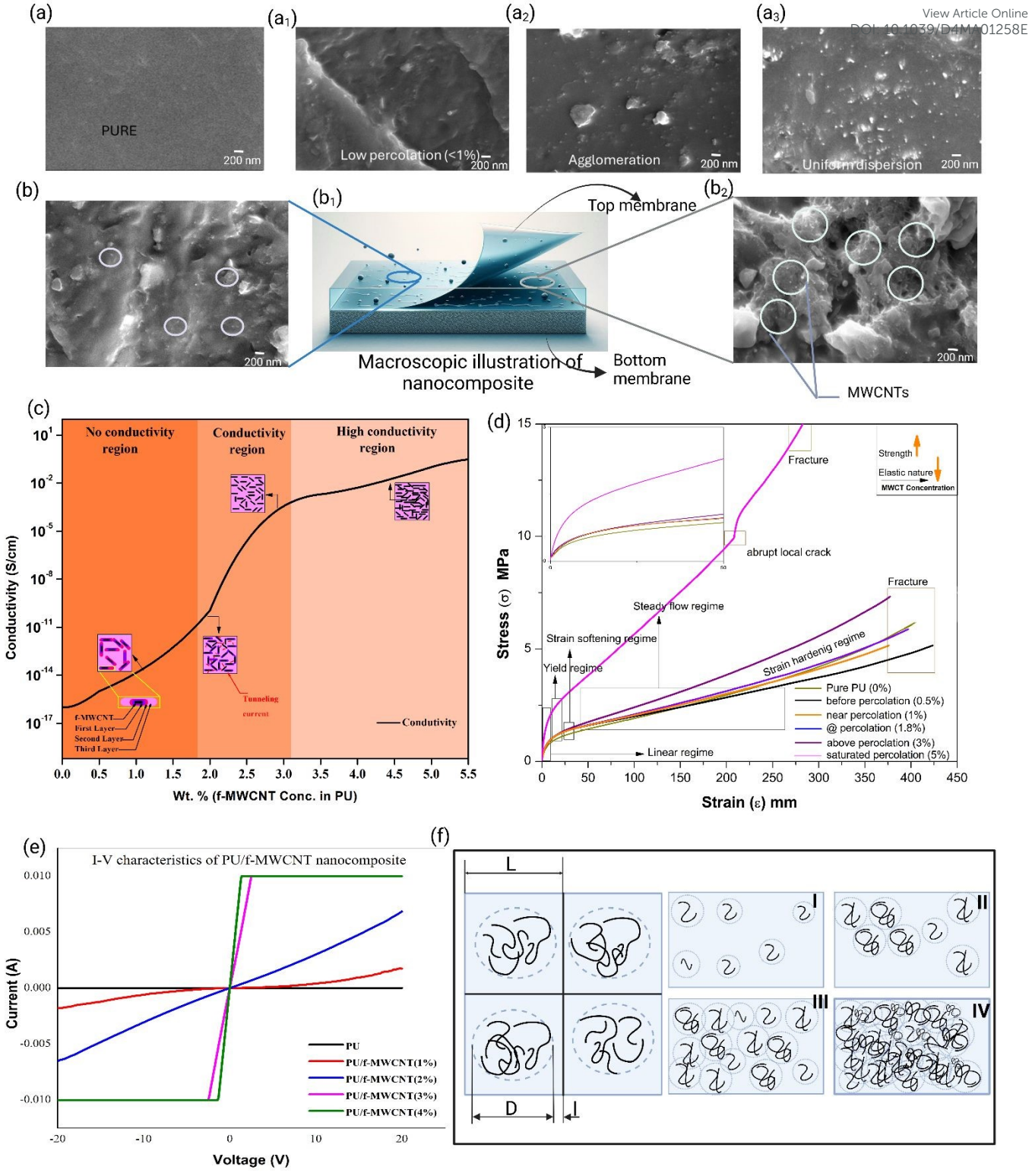

Figure 4:(a-a_3) shows SEM micrographs surface of nanocomposite at different filer loading conditions and (b-b_2) shows SEM micrographs of surface after removal of top membrane, (c) depicts the percolation curve of PU/f-MWCNTs nanocomposites (d) shows tensile study of nanocomposites (e) shows the I-V curves of PU/f-MWCNTs nanocomposites (f) illustration of interface of filler to polymer for electrical conduction

at around 1638 cm^{-1} was attributed to C=O bonding, which was not present in p-MWCNT [42]. This is correlated to carboxylate anion stretch mode. The peaks around 2400 cm^{-1} indicate the C-O bonding in f-MWCNTs [43]. The intensity of this peak was observed to be increased with HNO_3 concentration which could be attributed to the breakage of p-MWCNTs [44]. The peaks observed around 3750 cm^{-1} are attributed to hydroxyl groups present in f- MWCNTs [45]. From the figure 3 (b), it was

observed that O-H stretching was maximum for 4M HNO_3 treated f-MWCNTs, indicating a higher degree of carboxylation of MWCNTs. After functionalisation, due to introduction of -COOH, -OH groups and formation defects, MWCNTs exhibits lower decomposition temperature. This observed in TGA graphs as shown in figure 3 (c). Here, for p-MWCNTs and f-MWCNTs first step degradation occurs at 563 °C and 521 °C respectively. This lesser decomposition temperature for f-MWCNTs attributed to surface modifications on MWCNTs [46,47]. TEM micrographs shows clean, less entanglement and well defined morphology for f-MWCNTs than p-MWCNTs as shown in figure 3 (a_1-a_3). For the further experiments, 4M HNO_3 treated f-MWCNTs were selected based on FTIR analysis. Nanocomposites of p-MWCNTs and f-MWCNTs are incorporated with polyurethane (PU) using a magnetic stirrer using the solvent mixing technique [12]. The prepared nanocomposite of PU/p-MWCNT and PU/f-MWCNT are shown in Figure 3 (d_1-d_3). It was observed that p-MWCNTs unevenly agglomerated in the nanocomposites as shown in Figure 3 (d_2). However, f-MWCNTs in Figure 3 (d_3) and (d_4) showed better dispersion and lower agglomeration than p-MWCNTs nanocomposite. The uniform dispersion of f-MWCNTs in the polymer affects the resistance, as shown in Figure 3 (e). it was observed that compared to PU/p-MWCNTs, the PU/f-MWCNTs nanocomposites showed lower resistance due to better dispersion within the PU matrix. The nanocomposites treated with 4M nitric acid-treated f-MWCNTs nanocomposites showed lower resistance (6KΩ) compared to those with 2M nitric acid. According to FTIR analysis, f-MWCNTs treated with 4M HNO_3 possibly have higher carboxylic groups on MWCNTs, which increases the hydrophilicity and enhances the compatibility of MWCNTs with the polyurethane (PU) matrix by improving the interaction between the nanotubes and the polymer chains. This results in more uniform dispersion and lower electrical resistance of the nanocomposites.

To understand the effect of functionalization of MWCNTs on dispersion of MWCNTs in PU matrix, distribution of conductivity in the different regions of nanocomposites were studies. For this experiment, nanocomposites with a 5% f-MWCNT concentration were prepared. The two-point probe method was utilized to study the macroscopic electrical resistance of the nanocomposite. Nanocomposites were divided into eight equal parts, and resistance was measured as shown in Figure 3 (f). Experimental results revealed that resistivity across all regions of nanocomposites was uniform for nanocomposites treated with 4M HNO_3 compared to those with 2 M HNO_3. This could be attributed to uniform dispersion and stabilization of 4M HNO_3 treated f-MWCNTs in the matrix. From the dispersion and electrical characterization studies, we chose 4M HNO_3 treated f-MWCNTs for further experiments.

The surface morphology of PU/f—MWCNTs nanocomposite at different dispersion rate, was shown in figure 4 (a-a_3). Figure 4 (a) shows surface of Pure PU. Figure (a_1) shows f-MWCNTs dispersed at below electrical percolation threshold point. Figure (a_2) shows the agglomeration of f-MWCNTs induces clump like structure on PU. After optimised preparation conditions for nanocomposite, this agglomeration dispersed uniformly or decreases in diameter of agglomeration to disperse well in nanocomposite as shown in figure 4(a_3). To visible f-MWCNTs clearly, the top layer is removed and analysed SEM micrographs, as shown in illustration figure 4(b_1). The f-MWCNTs are covered on PU membrane can notice figure 4(b_2). This confirms, f-MWCNTs bonding in PU. Figure 4 (c) shows the percolation curve of PU/f-MWCNT nanocomposite. The percolation curve can be divided into three sections. In the first region of the curve, up to 1.8 wt% of f-MWCNTs, it was observed that the electrical conductivity was negligible. A considerable increase in electrical conductivity can be observed in the second region, from 1.8 wt% to 3.1wt % of f-MWCNTs. This can be attributed to the forming of electrical percolation paths in the nanocomposites. Therefore, 1.8 wt% of f-MWCNTs were considered as the Electrical Percolation Threshold (EPT) of the nanocomposite. The conductivity of the nanocomposite with 3.1 wt% of f-MWCNTs concentration was observed to be 0.01 S cm^{-1}.

Tensile experiments were conducted for analyse the change in strength of polymer and corelated to electrical percolation of nanocomposite as shown in figure 4(d). for this test, ASTM D-638 standard [48] were used and nanocomposites at different conducting scale was selected. Various tensile deformation mechanisms were studied for this experiment. Linear regime, where stress increasing linearly with strain, and its reversible. For Pure PU till 0.5 MPa, this linear regime was observed. This regime reducing with inclusion of f-MWCNT concentration in PU. However, stress is increasing as shown in inset figure 4 (d), that attributed to stiffness enhancement due to influence of f-MWCNTs. For yield regime, where nanocomposite deformation occurs for nucleation for plasticity. Results shows than Pure PU, all other nanocomposites range were increasing with increase in filler concentration. Then strain softening regime, with minimal load increasing in strain. For Pure PU, it was 1.03 MPa and observed that increase load transfer in this regime with inclusion of f-MWCNTs. For viscoelastic materials, after softening over stress, increase in strain happen with almost constant load, i.e steady state flow regime. Here, Pure PU exhibits 3.4 MPa of load transfer, however, at before percolation nanocomposites, shows i.e., 0.5 and 1 % shows 3.1 and 3.2 MPa respectively. However, at percolation nanocomposite i.e, 1.8% load transfer increased to 3.9 MPa. Above percolation nanocomposites i.e., 3 and 5% exhibits 4.3 and 7.8 MPa respectively. This increase in load transfer behaviour in this regime at and above 1.8% nanocomposites, attributed to filler materials are well-interconnected in matrix material. But decrease in load transfer for before percolation nanocomposites, due to not enough fillers dispersed to connect or make network In matrix, that disrupts load transfer. This leads to shortening in steady flow regime. But for PU, prolonged regime observed due its intrinsic viscoelastic nature [49]. This shows that after inclusion of filler materials at or above percolation concentration, makes nanocomposites increase in improved interfacial load transfer. In strain hardening regime, maximum load was observed. For Pure PU it was, 5.68 MPa, for 0.5% and 1% nanocomposites it decreased to 4.5 and 4.92 MPa respectively. For 1.8% nanocomposites 5.78 was observed. Above percolation nanocomposites, i.e., 3 and 5%s maximum load increased to 7.18 and 15 MPa. However, for after percolation nanocomposites, maximum load capacity increased but elastic regime was decreasing. By analysing, these

mechanisms, nanocomposites of around 1.8% f-MWCNTs are less affected for elastic nature and persists the basic matrix characteristics while adding conducing nature to polymer. This claims, evident by further electrical characterization.

The four-point probe method was used to obtain nanocomposites I-V(current-voltage) characteristics with different f-MWCNT concentrations. Figure 4 (e) shows the I-V curve for nanocomposite with f-MWCNT concentrations of 0%, 1%, 2%, 3%, and 4% in forward and reverse bias. The IV characteristics of Pure PU show almost flat, indicating that PU is an insulating material with very low current flow over the applied voltage range. For 1% f-MWCNTs, the curve shows a slight increase in current with applied voltage compared to pure PU, indicating some level of conductivity but still relatively low. For 2% f-MWCNTs, the curve shows a more noticeable increase in current with applied voltage, indicating higher conductivity than the 1% f-MWCNT composite. For 3% f-MWCNTs, the curve demonstrates a further increase in current, showing even higher conductivity. For 4% f-MWCNTs, the curve shows the highest current for a given voltage among all the samples, indicating the highest conductivity. Including f-MWCNTs in the PU matrix significantly enhances the electrical conductivity of the nanocomposites compared to pure PU. This improvement is more evident with increasing weight percentages of f-MWCNTs. At lower concentrations of f-MWCNTs (1% and 2%), the IV curves are less linear, possibly due to less effective percolation of the conductive network within the PU matrix. For higher concentrations of f-MWCNTs (3% and 4%), the IV curves show a more linear relationship, indicating ohmic behaviour where the current is proportional to the applied voltage. Above this concertation, the nanocomposite can be considered in the high conductivity region of the percolation curve. Figure 4(f) shows the interface formation due to the interaction between polymer chains and the surface of the f-MWCNTs. An increase in nanofiller concentration results in the overlap of interfacial layers, a conducting path will be developed, and polymer nanocomposites will show conductivity. Near the electrical percolation threshold, the electrical conductivity of a polymer nanocomposite is [50],

$$\boldsymbol{\sigma = \sigma_0(\varphi_f - \varphi_p)^s} \qquad (\mathbf{1})$$

where σ is the electrical conductivity of the nanocomposite, σ_o is the electrical conductivity of the filler particle, ϕ_p is the volume fraction of filler particles at the electrical percolation threshold (EPT), while ϕ_f is the volume fraction of filler particles. To understand the change in the conductivity of the PU/f-MWCNT nanocomposite to the strain, it is assumed that the agglomerates are distributed evenly in the matrix, as shown in figure 4(c). Also, the polymer matrix is assumed to be divided into cubic elements with a side length of L and f-MWCNT agglomerates are placed at the center of the cubic elements.

The length of each cube, $L = D + l$ (2)

Where D is the diameter of the agglomerate. l is the distance between two agglomerates at the percolation threshold ϕp . Dp is the diameter of the agglomerate at the percolation threshold. Df is the diameter of agglomerates at different concentrations. The volume of the interface region depends upon the type and strength of the interaction between f-MWCNT and the polymer matrix.

Hence, the volume fraction of CNT agglomerates at the percolation threshold will be,

$$\varphi_p = \frac{V_{agglomerate\ at\ percolation}}{V_{cube}} = \frac{\pi {D_p}^3}{6\left(D_p + l\right)^3} \qquad (3)$$

The volume fraction of CNT agglomerates above the percolation threshold will be,

$$\varphi_f = \frac{V_{agglomerate}}{V_{cube}} = \frac{\pi {D_f}^3}{6(D_p + l)^3} \qquad (4)$$

Hence, the conductivity above the percolation threshold can be written as,

$$\sigma = \sigma_0\left(\frac{\pi({D_f}^3 - {D_p}^3)}{6\left(D_p + l\right)^3}\right)^s \qquad (5)$$

For a specific volume percentage of f-MWCNT and above percolation threshold, equation (5) can be written as,

$$\sigma = \sigma_0\left(k\,(\frac{1}{\left(D_p + l\right)^3}\right)^s \qquad (6)$$

Where,

$k = \left(\frac{\pi({D_f}^3 - {D_p}^3)}{6}\right)$ is a constant independent of the strain applied to the nanocomposite.

The distance between the agglomerates (l) increases when the nanocomposite is stretched. Equation 6 suggests that the electrical conductivity decreases as the distance between the agglomerates above the percolation threshold increases. It can be observed that as the functionalisation increases, agglomeration reduces, and f-MWCNTs are dispersed polymer matrix. Therefore, it can be assumed that Dp, that is the diameter of agglomerates at the percolation threshold reduces for f-MWCNTs and because of that distance between agglomerates (l) also reduces. This leads to a reduction in the resistance of the PU/f-MWCNT polymer nanocomposites. Functionalization stabilises the MWCNTs and results in better dispersion of agglomerations (with a smaller diameter) in the polymer evenly, which helps in achieving uniform conductivity in nanocomposites as shown in SEM micrographs in figure 4 (b). Hence, equation 6 suggests that the ratio of Dp to Df is low to achieve a lower EPT value.

View Article Online
DOI: 10.1039/D4MA01258E

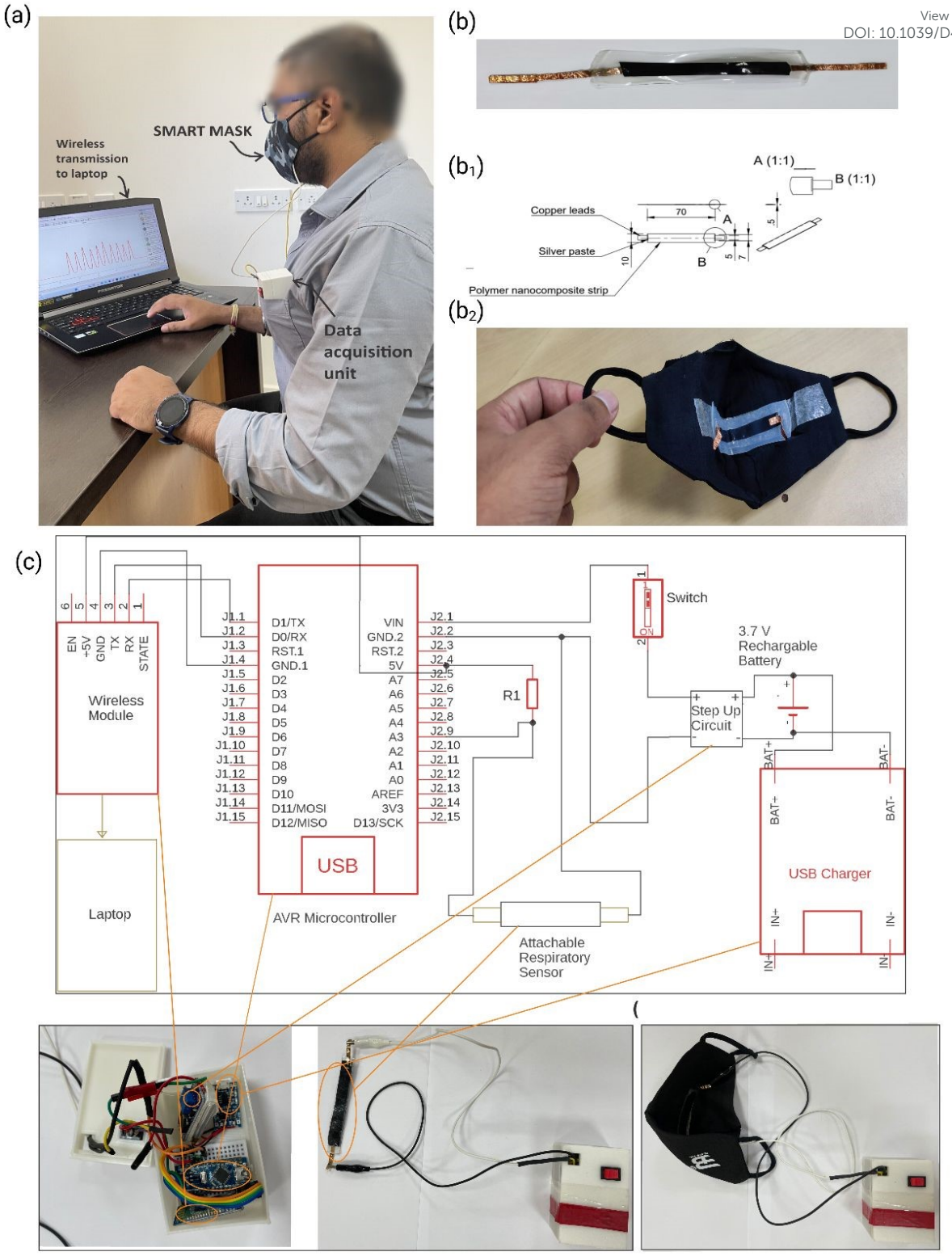

Figure 5: (a) shows sensor enabled mas wearing for test, (b-b_2) shows CAD model and sensor (c) depicts the circuit diagram for acquiring signals for fabrication of DAU

3.3. Development of face-mask attachable piezoresistive based Respiratory Sensor:

The prepared nanocomposite is attached to the face mask using double-sided tape as shown in figure 5 (a-b). In-house prepared signal acquisition setup connected to electrodes of nanocomposites. The circuit diagrams for acquiring signals are shown in Figure 5 (c). The components of the Data Acquisition Unit (DAU) are shown in

View Article Online
DOI: 10.1039/D4MA01258E

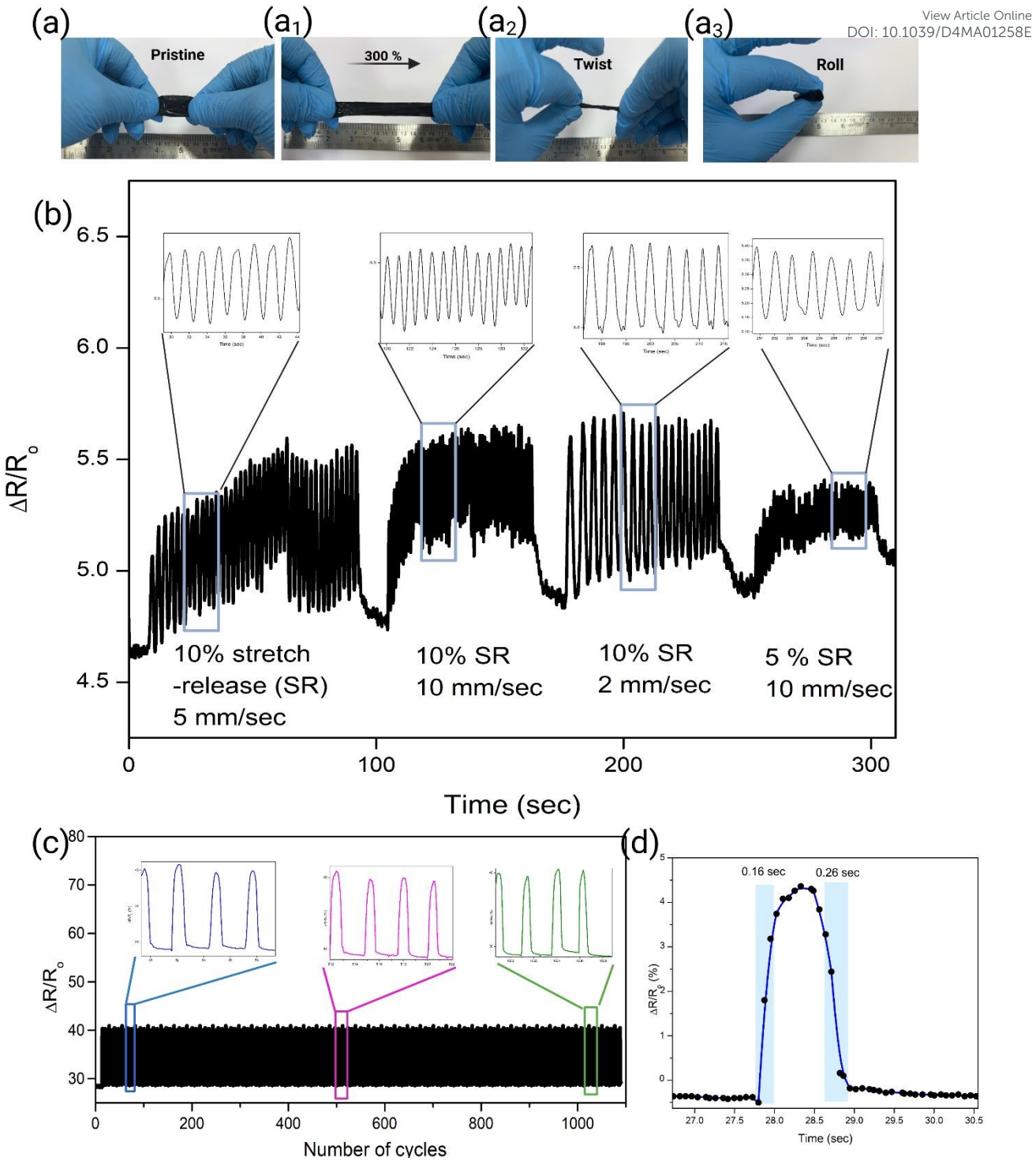

Figure 6: (a-a$_3$) shows sensors flexibility property, (b) shows real-time data of sensor stretch-release performance (c) shows sensitivity of sensor on prolonged time and (d) shows response time of senor.

Figure 5 (c). The DAU involves the AVR microcontroller (Arduino nano), battery to power the microcontroller, and Bluetooth module for wireless data transmission from Sensor enabled Mask (Figure 5) to laptop or mobile. The signal acquisition system was designed using an Arduino nano (ATPmega328P) processor with a voltage divider program. Megunolink was used to acquire wireless signals from nanosensor. Using the current acquisition system, sampling frequency of 128 points was recorded. After wearing the sensor-enabled mask, data is acquired and transferred wirelessly to the laptop for normal, slow, and fast breathing. The inflow and outflow of air from nostrils will induce the strain on the nanocomposite, disrupting the conductive path and resulting in a resistance change in the sensor. This change in resistance in the sensor is acquired and processed to analyse breathing patterns.

3.3.1. Sensor Parameters: Prepared sensor was studied for its performance under different conditions. This prepared sensor exhibits its flexibility, twistability and deform to different

View Article Online
DOI: 10.1039/D4MA01258E

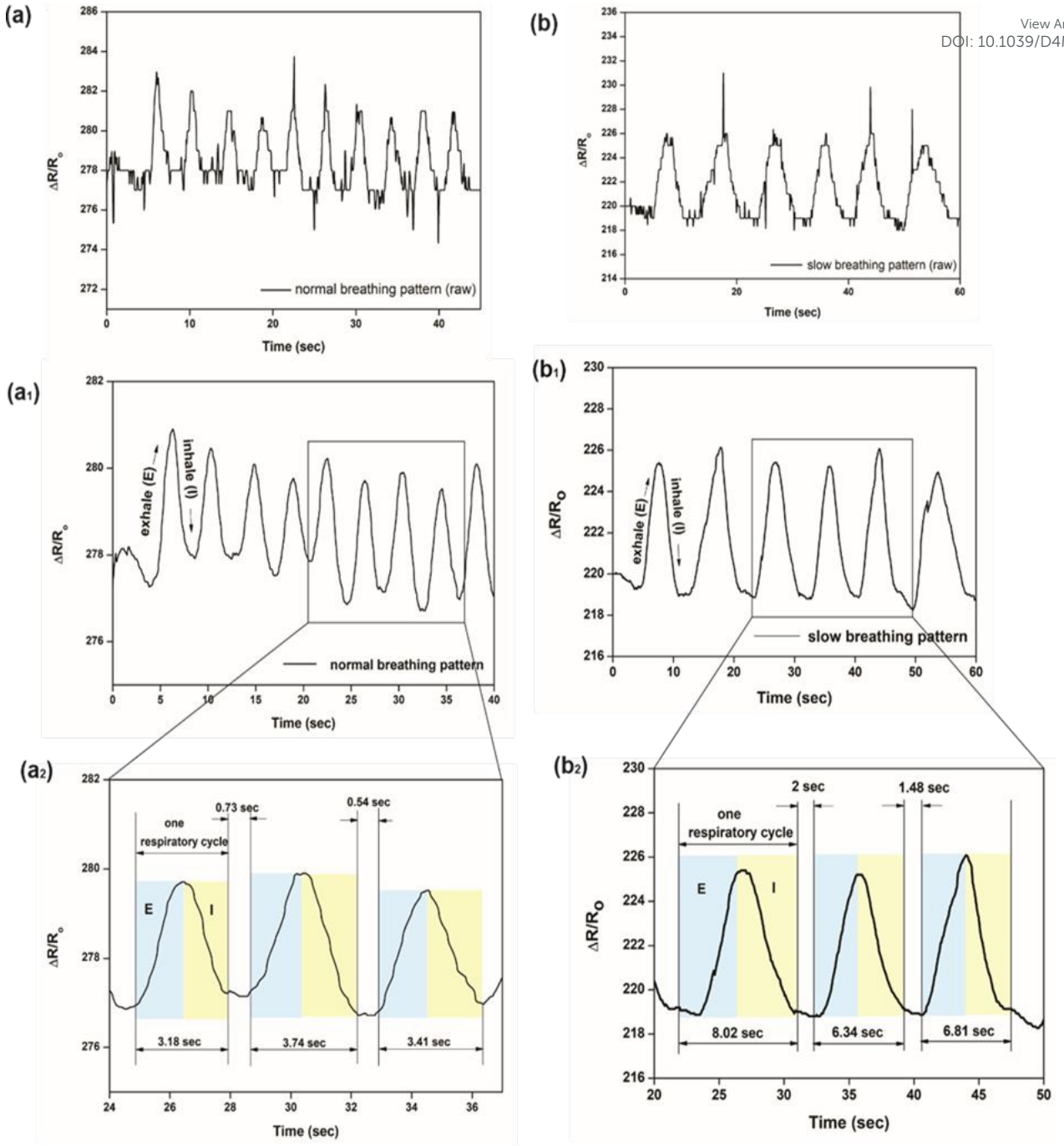

Figure 7: (a) shows the raw signal of normal breathing pattern (a_1) shows the processed of same signal with (a_2) its enlarged view with breathing parameters, (b) shows the raw signal of slow breathing with its (b_1) processed signals and enlarged(b_2) view of the same pattern with breathing parameters.

shapes without losing any pristine condition, as shown in figure 6 (a). figure 6 (b) shows real -time data acquisition of sensor at different stretch-release (SR) loading conditions. Initially sensor stretched for 10% at feed of 5 mm/sec, then increased to 10 mm/sec then shifted to 2 mm/sec and then, changed loading condition to 5% stretch at 10 mm/ sec. in all these different stretch and feed conditions, sensor able to detect all at real time as shown in figure 6 (b). further to see sensitivity of sensor, constant cyclic load of 10% strain performed for more than 1000 cycles, as shown in figure 6 (c). Response time for this sensor observed was 0.16 sec and 0.26 sec, shows real-time performance of the sensor as shown in figure 6 (d). Further sensor used for multiple applications.

3.4. Applications: Figure 7 (a, and b) demonstrates the respiratory patterns of individuals engaged in normal and slow breathing, acquired using sensor- enabled mask. The signals are processed using a low-pass filter with a cut-off frequency of 5Hz. In Figure 7 and Figure 8, the x-axis represents the time in seconds (sec) and the y axis represents the ratio of change in resistance ($\Delta R/R_o$).

View Article Online
DOI: 10.1039/D4MA01258E

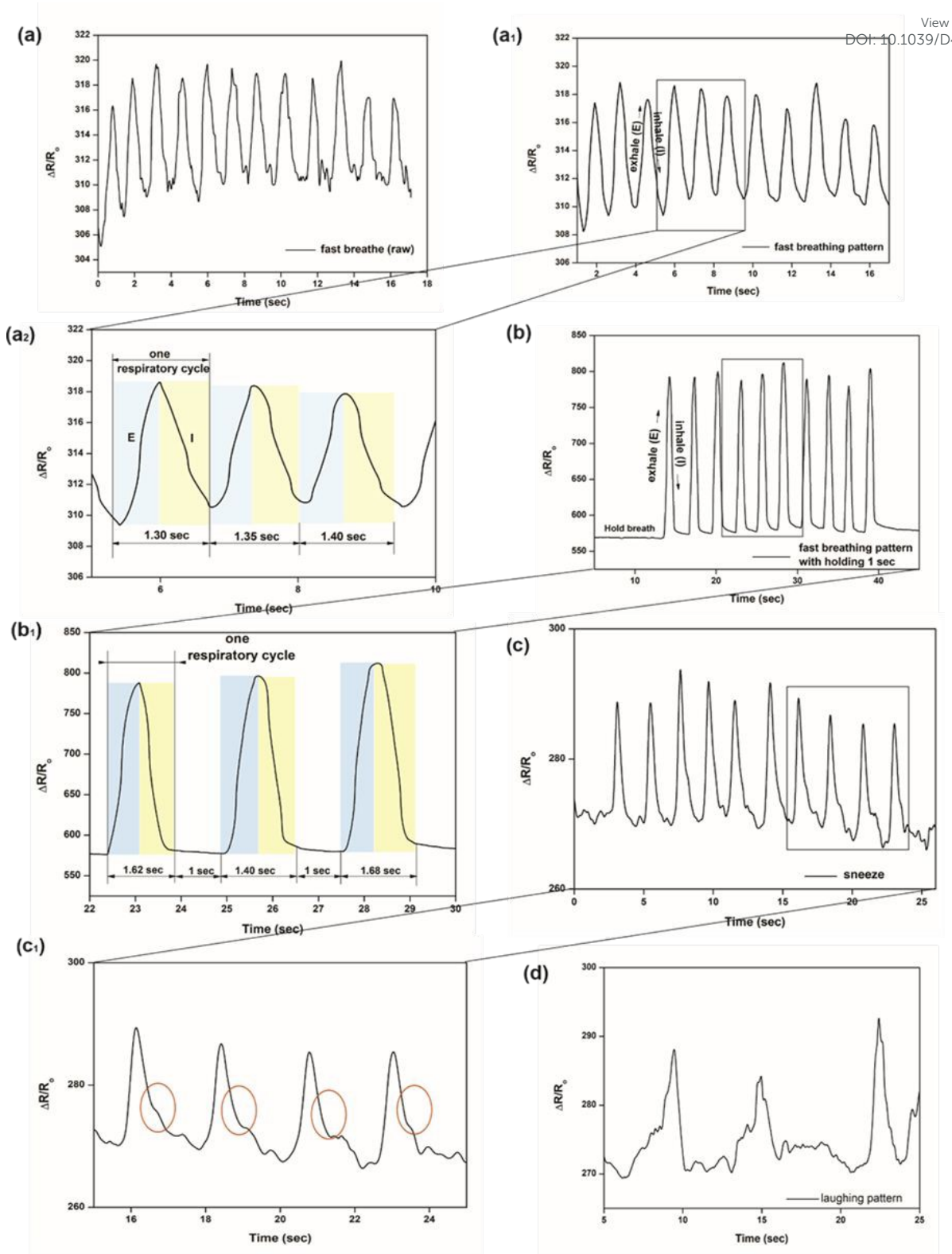

Figure 8: (a) shows the raw signal of fast breathing, (a_1) shows the processed signal of fast breathing with (a_2) enlarged view, (b) shows the fast breathing with hold of 1 sec and its (b_2) enlarged view, (c) shows the sneezing pattern with its (c_1) enlarged view and (d) shows the laughing pattern

For analysis, three respiratory cycles (including both exhalation and inhalation) were selected, as shown in Figure 7 (a_1, b_1). The average time required to complete one respiration cycle in the normal breathing pattern signal was 3.44 seconds, as demonstrated in Figure 7 (a_2). This pattern also exhibits the presence of a 0.73-second pause between consecutive respiration cycles, as depicted in the detailed view in Figure 7 (a_2). Similarly, for slow breathing patterns, as shown in Figure 7

View Article Online
DOI: 10.1039/D4MA01285E

(b) the time required to complete one respiration cycle increased to 7.05 sec on average, and the hold time between the cycles increased to 2 sec. The difference between normal and slow breathing patterns identifiable from the Figure 7 (a and b). Identifying respiratory signal patterns facilitates the determination of inhalation and exhalation durations and different breathing patterns.

This sensor- enabled mask can be used for real-time monitoring of respiratory activity in healthcare and sports applications. For instance, in healthcare applications, to monitor individuals with acute and chronic intrathoracic blockage during an asthma period by observing prolonged exhalation time. Similarly, an extended inspiration time Figure 7 (b_2) may indicate acute upper airway blockage. The advantage of this sensor enabled mask is that for many respiratory diseases, the patients generally show mouth breathing, which can be easily picked up by the developed sensor-enabled mask .

Furthermore, as demonstrated in Figure 8 (a, a_1), this sensor-enabled mask could obtain data on fast respiration. In fast breathing, data such as one respiration cycle requiring 1.35 seconds can be identified from the Sensor enabled mask signals, which was corroborated during the experiment with direct measurement. Further, we observed the absence of the hold time between cycles during fast respiration and the presence of hold time in normal and slow respiration, also identified in the signals acquired. Additionally, hold of breath during fast respiration was also performed and was detected and acquired by the sensor-enabled mask , as shown in Figure 8 (b, b_1). For this action, respiration time measured directly was the same to 1.60 seconds and then a hold time of 1 second, which can also be clearly observed in the acquired signal Figure 8 (b_1).

As shown in Figure 8, the developed sensor-enabled mask can help to understand insights into respiratory patterns such as hyperventilation. By continuously monitoring the user's breathing, the sensor-enabled mask can detect variations from normal respiratory rates and patterns, warning of potential

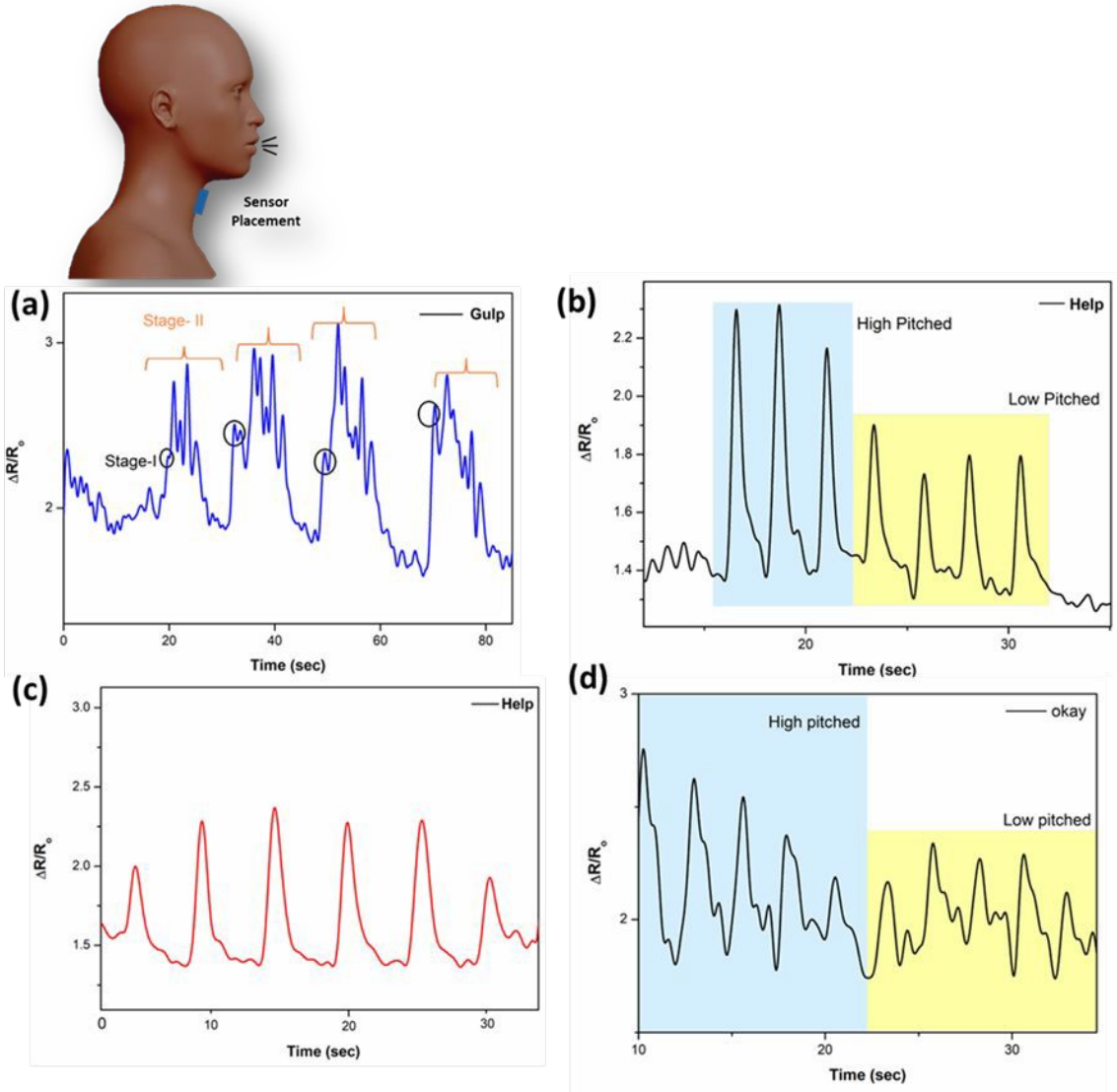

Figure 9: As Throat-mounted sensor, acquired (a) gulping action and vocal actions such as (b & c) HELP word at different voice pitched and (d) OKAY word

respiratory problems early.

Further, the sensor-enabled mask demonstrated the acquisition and distinguishing sneezing and laughing patterns through piezoresistive sensing. Figure 8 (c and d) illustrates these patterns with Figure 8 (c_1) providing an enlarged view of sneezing patterns. The data reveals a distinct peak within the normal respiratory signals, attributed to the abrupt pressure increase during a sneeze. This sudden pressure disrupts the conducting path, resulting in a noticeable peak in the sensor output.

3.4.1. Other Applications: Throat-mounted sensors can detect piezoresistive variations (fluctuations in electrical resistance) due to throat vibrations and pressure differences. This sensitivity enables the sensor to acquire real-time data on vocal activity, encompassing loudness, and pattern variations linked to speech or swallowing. To extend the capability of this sensor, sensor was attached to throat and acquired signals from gulping to speech actions as shown in figure 9. Figure 9 (a) shows the gulping action, When individual gulp or swallow, the voice box and surrounding muscles engage in coordinated that is initiated as shown stage- I. after that process, engaged in movements, resulting in the throat area to shift visibly and palpably as shown in stage- II. A sensor at the throat can pick up on the distinct patterns of these muscle contractions. by monitoring throat movement, individuals swallowing process can be identified. Again sensor positioned at the same position, and performed some speech actions. In figure 9 (b), the word 'HELP', repetitively voicing at high and low pitch was shown. In this signals we observe repetitive patterns for both high and low pitched voice. To ensure the repeatability, HELP word voiced in normal range, and observed repetitive and similar patterns as shown in figure 9 (c). similarly for OKAY word also voiced at high to low pitched voice and observed recurring patterns and distinct pattern from HELP word. These applications make this sensor assistive for technology for speech and communication.

4. Conclusion

The sensor-enabled mask demonstrates capturing and differentiating between normal and slow respiratory patterns, utilizing piezoresistive nanocomposite sensors. Respiratory patterns illustrate the distinct respiratory patterns obtained during normal and slow breathing. Analysis of respiratory cycles shows that the average duration for a normal breathing cycle is 3.44 seconds with a 0.73-second pause between cycles. In contrast, the slow breathing pattern exhibits a cycle duration of 7.05 seconds with a 2-second pause between cycles. These variations in respiratory patterns are clearly identifiable, enabling precise determination of inhalation and exhalation durations. Also, ability to detect specific respiratory events, such as sneezing, showcases the sensor-enabled mask potential as a sensitive and reliable tool for monitoring respiratory patterns and differentiating between various types of respiratory activities.

Continuous monitoring of respiratory health and breathing patterns can be beneficial for timely intervention or as data for diagnoses and understanding the patient recovery process. The paper aims to develop a real-time prototype to monitor patient respiratory health wirelessly. The development of wireless nanosensor strips is attachable and detachable to any mask. Continuous evaluation of breathing is possible. It will also provide information about patients' respiratory health, recovery, and health monitoring after recovery. This technology could be particularly valuable for health monitoring, offering a non-invasive and accurate method to track and analyze respiratory events in real time.

Author Contribution: Niranjan D B- Conceptualization, Data Curation, Formal Analysis, Funding Acquisition, Investigation, Methodology, Project Administration, Resources, Software, Supervision, Validation, Visualization, Writing – original draft, Writing – review & editing, Mathew Peter- Project Administration, Supervision, Validation, Writing – review & editing., Jeevan Medikonda- Project Administration, Supervision, Validation, Writing – review & editing, Pramod Kesavan Namboothiri- Formal Analysis, Funding Acquisition, Investigation, Methodology, Project Administration, Resources, Software, Supervision, Validation, Visualization, Writing – review & editing.

Conflicts of interest

There are no conflicts to declare

Data availability

All data supporting the findings of this study are available within the article and its Supplementary Information. Any additional data required to reproduce the results are available from the corresponding author upon reasonable request.

Funding Sources

This work supported by Indian council of Medical Research, ITR head (5/3/8/40/ITR-F/2022-ITR), Govt. of India, Anusandhan National Research Foundation, Govt. of India (SCP/2022/000264) and Manipal Academy of Higher Education.

Acknowledgements

We acknowledge research facilities provided by Central Instrumentation facility MAHE, Manipal and Sophisticated Test and Instrumentation center, Kochi, India. Niranjan acknowledges here Mr. Shamanth Madapur for valuable inputs on fabricating the circuit diagram for the data acquisition system. Niranjan D B, deeply grateful for the invaluable support provided by Vaidehi B R, whose wisdom continues to inspire me even in her absence.

Notes

This work has been filed for Indian patent, under number 202411041475.

Experimental Methods: Integration of f-MWCNTs to PU Matrix: To study the uniform dispersion of f-MWCNTs and its effects on electrical conductivity behaviour, nanocomposites of p-MWCNTs and f-MWCNTs are incorporated with polyurethane (PU) using a magnetic stirrer by solvent mixing technique and prepared nanocomposite of PU/p-MWCNT and PU/f-MWCNT from 1, 2, 2.5, 3, 4 and 5%. The water based PU polymer added with 5:1 ratio with DI water and stirred for 1 hr to make solution-1. In another beaker f-MWCNTs are bath sonicated with aid of water as solvent for an hour to disperse as solution-2. Now prepared f-MWCNT solution added drop by drop to solution-1. To enhance the integration of f-MWCNTs with PU matrix solution kept stirred for 12 hrs. Addition of f-MWCNT solution are added to solution 1 based on w/w% ratio for required concentration of nanocomposites. Then the solution was degassed in vacuum desiccator for 25 min and poured on clean glass petri dish of 80 cm dia. After that, solvent was allowed to evaporate in ambient conditions for 24 h to get thin film.

Preparation of nanocomposite to piezoresistive sensor: Optimized thin film from prepared nanocomposite cut into 70 mm x 10 mm x 0.15 mm dimensions to use as sensor. Copper-based electrodes were attached to selected nanocomposite using a silver paste to reduce the contact resistance. This piezoresistive sensor was positioned in the middle of the mask. Then, alligator clips are attached to the copper electrodes to connect the DAU.

References

1. Mai, Huy, Rahim Mutlu, Charbel Tawk, Gursel Alici, and Vitor Sencadas. "Ultra-stretchable MWCNT–Ecoflex piezoresistive sensors for human motion detection applications." Composites Science and Technology 173 (2019): 118-124.
2. Su, Y., Liu, Y., Li, W., Xiao, X., Chen, C., Lu, H., ... & Chen, J. (2023). Sensing–transducing coupled piezoelectric textiles for self-powered humidity detection and wearable biomonitoring. Materials horizons, 10(3), 842-851.
3. Mishra, S., & Saha, B. (2024). Graphene-polymer nanocomposite-based wearable strain sensors for physiological signal Monitoring: Recent progress and challenges. Current Opinion in Solid State and Materials Science, 31, 101174.
4. Alvarez-Fernandez, A., & Maiz, J. (2024). Advancements in polymer nanoconfinement: tailoring material properties for advanced technological applications. RSC Applied Polymers, 2(6), 1013-1025.
5. Wang, X., Li, H., Wang, T., Niu, X., Wang, Y., Xu, S., ... & Liu, H. (2022). Flexible and high-performance piezoresistive strain sensors based on multi-walled carbon nanotubes@ polyurethane foam. RSC advances, 12(22), 14190-14196.
6. Dhakal, K. N., Lach, R., Grellmann, W., Krause, B., Pionteck, J., & Adhikari, R. (2024). Piezoresistivity and strain-sensing behaviour of poly (butylene adipate-co-terephthalate)/multiwalled carbon nanotube nanocomposites. RSC advances, 14(48), 35715-35726.
7. Cai, Y., Liu, L., Meng, X., Wang, J., Zhang, C., Li, J., ... & Duan, J. A. (2022). A broad range and piezoresistive flexible pressure sensor based on carbon nanotube network dip-coated porous elastomer sponge. RSC advances, 12(52), 34117-34125.
8. Wang, S., Deng, W., & Yang, W. (2024). Superhydrophobic stretchable sensors based on interfacially self-assembled carbon nanotube film for self-sensing drag-reduction shipping. RSC advances, 14(36), 26505-26515.
9. Feng, Y., Cai, R., Zhou, Y., Hu, Z., Wang, Y., Liu, D., ... & Meng, Q. (2022). A high-performance porous flexible composite film sensor for tension monitoring. RSC advances, 12(40), 26285-26296.
10. Feng, J., Ao, H., Cao, P., Yang, T., & Xing, B. (2024). Flexible tactile sensors with interlocking serrated structures based on stretchable multiwalled carbon nanotube/silver nanowire/silicone rubber composites. RSC advances, 14(20), 13934-13943.
11. Ananthasubramanian, P., Sahay, R., & Raghavan, N. (2024). Investigation of the surface mechanical properties of functionalized single-walled carbon nanotube (SWCNT) reinforced PDMS nanocomposites using nanoindentation analysis. RSC advances, 14(22), 15249-15260.
12. Joo, D. H., Kang, M. S., Park, S. J., Yu, S. A., & Park, W. T. (2022). Fabrication method of flexible strain sensors with CNTs and solvents. Sensors and Actuators A: Physical, 345, 113775.
13. Bharadwaj, S., Gupta, T. K., Chauhan, G. S., Sehrawat, M., Kumar, A., Dhakate, S. R., & Singh, B. P. (2023). Long length MWCNT/TPU composite materials for stretchable and wearable strain sensors. Sensors and Actuators A: Physical, 357, 114364.
14. Liu, M. Y., Hang, C. Z., Wu, X. Y., Zhu, L. Y., Wen, X. H., Wang, Y., ... & Lu, H. L. (2022). Investigation of stretchable strain sensor based on CNT/AgNW applied in smart wearable devices. Nanotechnology, 33(25), 255501.
15. Hu, T., & Sheng, B. (2024). A highly sensitive strain sensor with wide linear sensing range prepared on a hybrid-structured CNT/Ecoflex film via local regulation of strain distribution. ACS Applied Materials & Interfaces, 16(16), 21061-21072.
16. Liu, L., Zhang, X., Xiang, D., Wu, Y., Sun, D., Shen, J., ... & Li, Y. (2022). Highly stretchable, sensitive and wide linear responsive fabric-based strain sensors with a self-segregated carbon nanotube (CNT)/Polydimethylsiloxane (PDMS) coating. Progress in natural science: materials international, 32(1), 34-42.
17. Liu, Y., Xiao, H., Pang, D., Sun, S., Sun, Z., & Liu, S. (2025). Hybrid structured wearable flexible piezoresistive sensor with high sensitivity and wide detection range. Sensors and Actuators A: Physical, 116520.
18. Nguyen, Thao, Michael Chu, Robin Tu, and Michelle Khine. "The effect of encapsulation on crack-based wrinkled thin film soft strain sensors." Materials 14, no. 2 (2021): 364.
19. Huang, J., Xie, G., Xu, X., Geng, Z., & Su, Y. (2024). Degradable multilayer fabric sensor with wide detection range and high linearity. ACS Applied Materials & Interfaces, 16(43), 58838-58847.
20. D'anna, Edoardo, Francesco M. Petrini, Fiorenzo Artoni, Igor Popovic, Igor Simanić, Stanisa Raspopovic, and Silvestro Micera. "A somatotopic bidirectional hand prosthesis with transcutaneous electrical nerve stimulation based sensory feedback." Scientific reports 7, no. 1 (2017): 10930.
21. Choi, Suji, Sang Ihn Han, Dongjun Jung, Hye Jin Hwang, Chaehong Lim, Soochan Bae, Ok Kyu Park et al. "Highly conductive, stretchable and biocompatible Ag–Au core–sheath nanowire composite for wearable and implantable bioelectronics." Nature nanotechnology 13, no. 11 (2018): 1048-1056.
22. Lee, Hee Young, Heidy Cruz, and Younggon Son. "Effects of incorporation of polyester on the electrical resistivity of polycarbonate/multi-walled carbon nanotube nanocomposite." Journal of Composite Materials 53, no. 10 (2019): 1291-1298
23. Zhang, Yi-Zhou, Kang Hyuck Lee, Dalaver H. Anjum, Rachid Sougrat, Qiu Jiang, Hyunho Kim, and Husam N. Alshareef. "MXenes stretch hydrogel sensor performance to new limits." Science advances 4, no. 6 (2018): eaat0098.
24. Sohrabi, Catrin, Zaid Alsafi, Niamh O'Neill, Mehdi Khan, Ahmed Kerwan, Ahmed Al-Jabir, Christos Iosifidis, and Riaz Agha.

"Corrigendum to "World health organization declares global emergency: a review of the 2019 novel coronavirus (COVID-19)"[int. J. Surg. 76 (2020) 71–76]." International journal of surgery 77 (2020): 217.
25. Imran, Ali, Iryna Posokhova, Haneya N. Qureshi, Usama Masood, Muhammad Sajid Riaz, Kamran Ali, Charles N. John, MD Iftikhar Hussain, and Muhammad Nabeel. "AI4COVID-19: AI enabled preliminary diagnosis for COVID-19 from cough samples via an app." Informatics in medicine unlocked 20 (2020): 100378.
26. Paraguassu, Eber Coelho, Huijun Chen, Fei Zhou, Zhe Xu, and Meiyun Wang. "Coronavirus and COVID-19: The latest news and views from the scientific community about the new coronavirus and COVID-19." Brazilian Journal of Implantology and Health Sciences 2, no. 3 (2020): 96-109.
27. Wang, Yixuan, Yuyi Wang, Yan Chen, and Qingsong Qin. "Unique epidemiological and clinical features of the emerging 2019 novel coronavirus pneumonia (COVID-19) implicate special control measures." Journal of medical virology 92, no. 6 (2020): 568-576.
28. Criée, C. P., S. Sorichter, H. J. Smith, P. Kardos, R. Merget, D. Heise, D. Berdel et al. "Body plethysmography–its principles and clinical use." Respiratory medicine 105, no. 7 (2011): 959-971.
29. Konno, Kimio, and Jere Mead. "Measurement of the separate volume changes of rib cage and abdomen during breathing." Journal of applied physiology 22, no. 3 (1967): 407-422.
30. Massaroni, Carlo, Elena Carraro, Andrea Vianello, Sandra Miccinilli, Michelangelo Morrone, Irisz K. Levai, Emiliano Schena et al. "Optoelectronic plethysmography in clinical practice and research: a review." Respiration 93, no. 5 (2017): 339-354.
31. Caretti, David M., Paul V. Pullen, Leslie A. Premo, and Wade D. Kuhlmann. "Reliability of respiratory inductive plethysmography for measuring tidal volume during exercise." American Industrial Hygiene Association Journal 55, no. 10 (1994): 918-923.
32. Khan, Yasser, Aminy E. Ostfeld, Claire M. Lochner, Adrien Pierre, and Ana C. Arias. "Monitoring of vital signs with flexible and wearable medical devices." Advanced materials 28, no. 22 (2016): 4373-4395.
33. Wang, Yan, Li Wang, Tingting Yang, Xiao Li, Xiaobei Zang, Miao Zhu, Kunlin Wang, Dehai Wu, and Hongwei Zhu. "Wearable and highly sensitive graphene strain sensors for human motion monitoring." Advanced Functional Materials 24, no. 29 (2014): 4666-4670.
34. Laukhina, Elena, Raphael Pfattner, Lourdes R. Ferreras, Simona Galli, Marta Mas-Torrent, Norberto Masciocchi, Vladimir Laukhin, Concepció Rovira, and Jaume Veciana. "Ultrasensitive Piezoresistive All-Organic Flexible Thin Films." Advanced Materials 22, no. 9 (2010): 977-981.
35. Amjadi, Morteza, Ki-Uk Kyung, Inkyu Park, and Metin Sitti. "Stretchable, skin-mountable, and wearable strain sensors and their potential applications: a review." Advanced Functional Materials 26, no. 11 (2016): 1678-1698.
36. Mai, Huy, Rahim Mutlu, Charbel Tawk, Gursel Alici, and Vitor Sencadas. "Ultra-stretchable MWCNT–Ecoflex piezoresistive sensors for human motion detection applications." Composites Science and Technology 173 (2019): 118-124.
37. Hoa, L. Thi Mai. "Characterization of multi-walled carbon nanotubes functionalized by a mixture of HNO3/H2SO4." Diam. Relat. Mater 89 (2018): 43-51.
38. Ahmed, Duha S., Adawiya J. Haider, and M. R. Mohammad. "Comparison of functionalization of multiwalled carbon nanotubes treated by oil olive and nitric acid and their characterization." Energy Procedia 36 (2013): 1111-1118
39. Gómez, Sofía, Nicolás M. Rendtorff, Esteban F. Aglietti, Yoshio Sakka, and Gustavo Suárez. "Surface modification of multiwall carbon nanotubes by sulfonitric treatment." Applied Surface Science 379 (2016): 264-269.
40. Osorio, A. G., I. C. L. Silveira, V. L. Bueno, and C. P. Bergmann. "H2SO4/HNO3/HCl—Functionalization and its effect on dispersion of carbon nanotubes in aqueous media." Applied Surface Science 255, no. 5 (2008): 2485-2489.
41. Shanmugharaj, A. M., J. H. Bae, Kwang Yong Lee, Woo Hyun Noh, Se Hyoung Lee, and Sung Hun Ryu. "Physical and chemical characteristics of multiwalled carbon nanotubes functionalized with aminosilane and its influence on the properties of natural rubber composites." Composites Science and technology 67, no. 9 (2007): 1813-1822.
42. Hwa, K. Y., & Sharma, T. S. K. (2020). Nano assembly of NiFe spheres anchored on f-MWCNT for electrocatalytic reduction and sensing of nitrofurantoin in biological samples. Scientific reports, 10(1), 12256.
43. Sobha, A. P., & Sreekala, P. S. (2017). Electrical, thermal, mechanical and electromagnetic interference shielding properties of PANI/FMWCNT/TPU composites. Progress in Organic Coatings, 113, 168-174.
44. Stobinski, L., Lesiak, B., Kövér, L., Tóth, J., Biniak, S., Trykowski, G., & Judek, J. (2010). Multiwall carbon nanotubes purification and oxidation by nitric acid studied by the FTIR and electron spectroscopy methods. Journal of alloys and compounds, 501(1), 77-84.
45. Sarkar, N., Sahoo, G., & Swain, S. K. (2017). Nanocomposites of polyurethane filled with CNTs. In Polyurethane Polymers (pp. 191-219). Elsevier.
46. Le, T. M. H., Vo, N. D. H., Dang, D. M. T., & Doan, T. C. D. (2024). Effect of MWCNTs surface functionalization on the characterization of PVA/MWCNTs nanocomposites. Physica Scripta, 99(7), 075901.
47. Kumar, D., & Jindal, P. (2019). Effect of multi-walled carbon nanotubes on thermal stability of polyurethane nanocomposites. Materials Research Express, 6(10), 105336.kumar
48. ASTM, D. (2014). ASTM D-638. Standard test method for tensile properties of plastics. ASTM Int.
49. Liu, H., Wu, F. Y., Zhong, G. J., & Li, Z. M. (2023). Predicting the complex stress-strain curves of polymeric solids by classification-embedded dual neural network. Materials & Design, 227, 111773.
50. Ji, S. H., Lee, D., & Yun, J. S. (2021). Experimental and theoretical investigations of the rheological and electrical behavior of nanocomposites with universal percolation networks. Composites Part B: Engineering, 225, 109317.

View Article Online
DOI: 10.1039/D4MA01258E

Data Availability Statement

All data has been uploaded in supporting information file.